



저작자표시-비영리-변경금지 2.0 대한민국

이용자는 아래의 조건을 따르는 경우에 한하여 자유롭게

- 이 저작물을 복제, 배포, 전송, 전시, 공연 및 방송할 수 있습니다.

다음과 같은 조건을 따라야 합니다:



저작자표시. 귀하는 원저작자를 표시하여야 합니다.



비영리. 귀하는 이 저작물을 영리 목적으로 이용할 수 없습니다.



변경금지. 귀하는 이 저작물을 개작, 변형 또는 가공할 수 없습니다.

- 귀하는, 이 저작물의 재이용이나 배포의 경우, 이 저작물에 적용된 이용허락조건을 명확하게 나타내어야 합니다.
- 저작권자로부터 별도의 허가를 받으면 이러한 조건들은 적용되지 않습니다.

저작권법에 따른 이용자의 권리는 위의 내용에 의하여 영향을 받지 않습니다.

이것은 [이용허락규약\(Legal Code\)](#)을 이해하기 쉽게 요약한 것입니다.

[Disclaimer](#)

이학석사 학위논문

실리카 나노입자의 표면전하가  
세포내 시공간 분포 및 상호작용에  
미치는 영향에 대한 연구

Influence of surface charge on the intracellular spatio-temporal  
distribution and interaction of silica nanoparticles

울 산 대 학 교 대 학 원

의 과 학 과

신 연 희

Influence of surface charge on the intracellular  
spatio-temporal distribution and interaction  
of silica nanoparticles

지도교수 백찬기

이 논문을 이학석사학위 논문으로 제출함

2022년 2월

울산대학교 대학원

의과학과

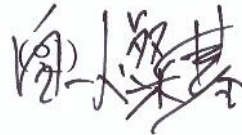
신연희

신연희의 이학석사학위 논문을 인준함

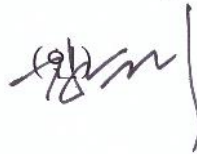
심사위원 하 창 훈 (인)



심사위원 백 찬 기



심사위원 김 준 기



울 산 대 학 교 대 학 원

2022년 2월

## Abstract

Nanoparticles are emerging as an effective drug carrier in drug delivery systems that can artificially control physicochemical properties. Among the physicochemical properties of nanoparticles, the surface charge is one of the key factors to be considered for efficient cell delivery. In particular, it is necessary to sufficiently consider which of the positive or negative surface charges is suitable for efficient intracellular delivery with low cytotoxicity. Recently, it demonstrated that various nanoparticles induce autophagy. However, it is still unclear how the induction of autophagy and the physicochemical properties of nanoparticles are quantitatively related to each other. In order to demonstrate this quantitative relationship at the level of single nanoparticles and organelles, this study investigated intracellular uptake, intracellular spatiotemporal distribution, and interactions with organelles, especially autophagosome, using silica-based fluorescent magnetic nanoparticles (Si-FMNPs) containing RITC dyes with different surface charges. As a result of spatio-temporal analysis of live cells using super-resolution confocal laser scanning microscopy (CLSM/Airyscan), Si-FMNPs with a positive charge (Si-FMNP/APTES) had higher intracellular uptake efficiency than Si-FMNPs with a negative charge (Si-FMNP/OH). Moreover, it was demonstrated that the kinetic properties of uptake, autophagy, and degradation processes were significantly different depending on the charge of the nanoparticles. In addition, it was also confirmed that the cytotoxicity of Si-FMNPs having a positive surface charge was remarkably low. Meanwhile, the refractive index (RI) value of each organelle of living cells was evaluated at the organelle level in real time using 3D label-free optical diffraction tomography (ODT). Interestingly, it was found that the RI values significantly increased in the nucleolus and the ER around the nucleus after nanoparticle treatment. These results are presumed to be caused by the accumulation of nanoparticles in the ER around the nucleus while interacting with autophagy, and physical changes in the nucleolus due to stress. This technique can be applied to analyze

the entire process of uptake and degradation into cells by treating nanoparticles or exosomes with a high refractive index without fluorescence in the future. This study, which quantitatively analyzed intracellular spatiotemporal analysis of nanoparticles by integrating high-resolution fluorescence and label-free imaging, is expected to greatly contribute to the development of an effective and safe nanocarrier.

**Key Words: Silica-based nanoparticles, surface charge, uptake and autophagic kinetics, optical diffraction tomography, refractive index**

# Contents

Abstract	i
List of figures	iv
List of tables	iv
1. Introduction	1
2. Materials and methods	5
3. Results	10
3.1 Characterization of the Si-FMNPs	10
3.2 Effect of silica nanoparticles on cell viability	14
3.3 Quantitative analysis of autophagy induced by Si-FMNP/OH and Si-FMNP/APTES	16
3.4 Spatio-temporal change of the cellular RI values induced by Si-FMNPs	29
4. Discussion	31
5. Conclusion	33
6. References	34
7. Supplementary data	42
국문 요약	45

## List of Figures

Figure. 1 Characterization of the Si-FMNPs .....	12
Figure. 2 Effect of nanoparticles on cell viability in MCF7 cells .....	15
Figure 3. Immunofluorescence staining images of autophagy-induced MCF7 cells .....	17
Figure. 4 Quantitative analysis of each fluorescent vesicles in the confocal image .....	23
Figure 5. Spatio-temporal time change of the cellular RI values induced by Si-FMNPs.....	25
Figure S1. Distribution of diameter and zeta potential of nanoparticles measured by dynamic light scattering (DLS) .....	42
Figure S2. Distribution of diameter and zeta potential of nanoparticles measured by Nanoparticle Tracking Analysis (NTA) .....	43
Figure S3. Confirmation of ER region using ER tracker imaging combined with RI mapping .....	44

## List of Tables

Table 1. Diameter, zeta potential of Si-FMNPs .....	12
Table 2. Mean refractive index (RI) of cellular organelles .....	28

# 1. Introduction

Nanomaterials in medicine are applied as biomedical tools in fields of diagnostic, monitoring, and therapy [1-5]. Nanoparticles (NPs) have the potential to improve safety and efficacy by increasing the stability and solubility of cargos and facilitating transport through membranes [6, 7]. Some successful nanomedicine has already appeared in today's pharmaceutical market and shown better clinical performance than conventional drugs [8]. Nanoparticles are used as drug carriers due to their variable physicochemical properties [9-11]. Practically, the physical and chemical properties of nanoparticles, such as size, shape, polydispersity, charge, and surface hydrophobicity/hydrophilicity, influence their biological responses [12-14]. Among numerous physicochemical properties, the charge of surface has been proposed as one of the major factors controlling numerous biological responses. It has been reported that the uptake of positively charged nanoparticles into MCF-7 cells was better than negatively charged nanoparticles, but did not affect human umbilical vein endothelial cells [15]. Also, it has been proposed that the amount of internalized fluorophore-conjugated polystyrene nanoparticles (F-PLNPs) was proportional to the zeta potential of F-PLNP in non-phagocytic A549 cells and HePG2 and phagocytic differentiated THP-1 cells [12]. According to these previous studies, positively charged nanoparticles seem to exhibit higher cellular uptake than negatively charged nanoparticles. In order to evaluate the efficacy of the drug delivery system, not only the extent to which nanoparticles are uptaken into cells but also the extent to which they accumulate in various organelles after uptake and the efficiency of drug release should be considered. In addition, since it is important not to induce toxicity to the cells during a series of interactions with organelles, it should be properly degraded after a certain period of time in the cells.

Among the various nanoparticles, silica-based particles (Si-NPs) are one of the effective nanomaterials due to their tunable diameter, easy surface modification, and robust dye payload [16-18]. Practically, Si-NPs have been used mainly to disperse poorly insoluble therapeutic

agents in aqueous media [19]. While Si-NPs have been utilized in numerous biomedical applications [20-25], analysis of the cellular uptake process in single-cell has been only limited to tumor treatment [26-28]. In general, in the case of oral administration of a drug, the drug is absorbed into the body through the digestive tract and spreads throughout the body along the bloodstream to reach target cells. After reaching the target cell, the drug enters the cell through endocytosis [29]. The effectiveness of drugs is evaluated by analyzing their effects on living bodies, organs, cells, and organelles. However, unlike the evaluation of living organisms or organs, studies on the effects of drugs other than target organelles or molecules in cells are insufficient.

Recently, it was found that various nanoparticles induce autophagy [30-34]. Autophagy is a ubiquitous process in eukaryotic cells that results in the disruption of cytoplasm within the lysosome in response to stressful conditions and that permits the cell to adjust to changes [35]. In the process of autophagy, the mediator of a double membrane-bound vesicle, referred to as an autophagosome, transports cytoplasmic cargo to the lysosome and then fuses with the lysosome to develop an autolysosome [36]. Previous studies have mainly focused on the intracellular uptake and the cytotoxicity of NPs [12, 15]. There are few studies that have focused on changes in spatiotemporal distribution, interactions of NPs with organelles, and degradation, which are key parameters for entirely understanding nanoparticles with different physicochemical properties as a drug carrier at the single-cell level.

Lately, optical diffraction tomography (ODT), one of the label-free quantitative phase imaging (QPI) methods, has arisen as a label-free three-dimensional (3D) imaging technique capable of measuring the volume and refractive index (RI) distribution of biological samples at a high spatial resolution [37, 38]. The ODT technique has been proposed as a prospective method for live cell imaging, which can overcome the limitations of fluorescence imaging [37, 39, 40], although the 3D image quality of organelles has not yet been completely compared

between confocal laser scanning microscopy (CLSM) and ODT. Since RI is an inherent optical property of the biomaterial, there is no need to use Romanowsky-Giemsa/hematoxylin-eosin staining agents or fluorescent labeling agents such as methylene blue, eosin, and fluorophore for cell imaging. In addition, it has the feature of high-speed imaging of 3D images of fixed cells as well as living cells. Because ODT reconstructs the 3D RI distribution (i.e. the 3D molecular density distribution) of a sample in a complex optical field measured by considering light diffraction inside the sample, ODT can be utilized to visualize the complicated structure of a sample [41]. Therefore, ODT may be useful for detecting the intracellular distribution of nanoparticles with a high value of RI or local changes in intracellular RI value caused by nanoparticles.

In this study, systematic evaluations were conducted to prove the hypothesis that the spatio-temporal intracellular distribution and organelle interactions (i.e. uptake and degradation process) of silica-based fluorescent magnetic nanoparticles containing RITC dye (Si-FMNPs) with different surface charges would be different. Firstly, the physical and electrostatic characteristics of Si-FMNPs were fully investigated using transmission electron microscopy (TEM), dynamic light scattering (DLS), and nanoparticle tracking analysis (NTA) in addition to measurement of zeta potential. Secondly, based on the super-resolution CLSM technique (Airyscan), the 3D of intracellular Si-FMNPs and autophagosomes was quantitatively analyzed. It should be noted that in the case of imaging analysis using fluorescence, only labeled nanoparticles and autophagosome/lysosome-related molecules are observed, and information on other organelles cannot be obtained. Lastly, the intracellular distribution of Si-FMNPs and the RI value of organelles such as the nucleolus, cytosol, and endoplasmic reticulum (ER) using ODT correlated with fluorescence microscopy were evaluated to detect any local changes in intracellular RI value caused by nanoparticles. Through the evaluations, this study elucidates that the amount and distribution of Si-FMNPs in MCF-7 breast cancer cells according to different surface charges progressed differently over time. Moreover, it was

found that there is also a difference in the kinetic property of autophagosomes and lysosome induction. Our study will contribute to the basis of drug delivery systems and further to the evaluation of drugs at the single-cell level.

## 2. Materials and Methods

### 2.1. Materials.

The silica-based fluorescent magnetic nanoparticles containing RITC dye (Si-FMNP; NEO-STEM™ TMSR50) were purchased from Biterials (Seongnam, Korea). For changing of surface charge, the Si-FMNPs were coated using (3-aminopropyl) triethoxysilane (APTES; Sigma-Aldrich, USA). To remove the preservative, the Si-FMNPs solution was centrifuged (12,000rpm, 10min, at room temperature). The solution of Si-FMNPs was washed in 90% ethanol and isolated by centrifugation (12,000rpm, 5min, at room temperature). The Si-FMNPs solution was washed with 90% ethanol and separated by centrifugation (12,000 rpm, 5 min, room temperature). After that, the Si-FMNPs solution with 100% ethanol is repeated once more. The samples were treated with a mixture of 100% ethanol and 50 $\mu$ l APTES solution per 30 $\mu$ g of nanoparticles having a volume of 1 ml overnight at room temperature. The samples were washed in 100% ethanol and isolated by centrifugation (12,000rpm, 5min, at room temperature) with three repetitions. Finished washing, the samples were made to have a volume of 1 ml in distilled water (D.W) or Dulbecco's Phosphate Buffered Saline (PBS) (Biowest, Nuaille', France).

### 2.2. Cell culture and Si-FMNPs treatment

Human breast cancer (MCF7) cells were cultured in RPMI 1640 (Biowest, Nuaille', France) containing 10% FBS and 1% of penicillin and streptomycin. Cell culture were incubated at 37°C in a humidified atmosphere containing 5% CO<sub>2</sub>. The Si-FMNPs were treated at a concentration of 0.2 mg/ml in cells for 1 hour and then washed in PBS with three repetitions. After that, the cells in media were confirmed at 0, 1, 3, 5, and 10 hours and treated at the same concentration and time in all experiments.

### *2.3. Immunofluorescence staining*

The cells were incubated with a solution (0.2mg/mL) of Si-FMNPs for 0h, 1h, 3h, 5h, and 10h in 20mm glass-bottom culture dish (NEST Scientific Inc. NJ, USA). The cells treated Si-FMNPs were fixed with 4% paraformaldehyde (PFA) in 0.1M PBS : media (1:1) for 5 min at 37°C, and fixed again with 4% PFA in 0.1M PBS for 5 min at R.T. After fixation, the samples were washed with PBS and rinsed with D.W. The samples were treated with 0.01M sodium citrate buffer (pH 6.0) and 0.1% triton x-100 and 0.05% tween 20 in 0.01M sodium citrate buffer (pH 6.0) to retrieve antigen. The samples were washed and blocked with PBS washing buffer (0.01M sodium phosphate buffer, pH 7.2 1% BSA, 1% NGS, 0.25% Tween 20, and 0.9% NaCl). After washing, the samples were incubated for overnight with the primary antibodies (LAMP1 (Cell signaling, Massachusetts, USA) and LC3B (Cell signaling, Massachusetts, USA)) diluted 1:150 in blocking solution. After washing with blocking solution, the samples were incubated for 2h with the secondary antibodies (Alexa fluor 647 (Life technologies, California, USA) and Alexa fluor 488 (Life technologies, California, USA)) diluted 1:300 in blocking solution. The nucleus was counterstained with DAPI (1:1000) (Invitrogen, Oregon, USA). After rinsing of D.W., samples were mounted with DAKO Fluorescence Mounting Medium (DAKO, CA, USA) and imaged using confocal laser scanning microscopy (CLSM; LSM880, Carl Zeiss, Germany).

### *2.4. Confocal laser scanning microscopy and IMARIS analysis*

Immunofluorescent stained cells were observed using an inverted confocal laser scanning microscope (LSM880 equipped with an Airyscan super-resolution imaging module; Carl Zeiss, Germany). Alexa fluor 647-tagged LAMP1 was excited at the 633nm wavelength and detected on a 645nm long-pass filter. Nanoparticles containing RITC were excited at the 561nm wavelength and detected on 570 to 620nm filters. Alexa fluor 488-tagged LC3B was excited at the 488 nm wavelength and detected on 495 to 550nm filters. The z-stack images were taken

at 0.5  $\mu$ m intervals using an objective lens (C-Apochromat, 63x/1.2 NA; Carl Zeiss). LSM observations were conducted at room temperature. Images acquired using LSM880 were processed by ZEN software and analyzed using IMARIS ver.8.1.2 software (Bitplane, Belfast, USA). The spot and colocalization function in the IMARIS software was used to analyze the counting and diameter of each fluorescent vesicle (i.e. bright puncta).

### *2.5. Label-free ODT*

The cells were cultured in 50 $\pi$  Tomo-Dish (Tomocube, Daejeon, Korea) for the ODT experiment. ODT was implemented as previously described [42, 43]. ODT transmits a laser beam 360 degrees to the sample to obtain 2D holographic images of the sample from multiple angles and then reconstructs them to create a 3D RI tomography image of the sample. [44]. The ODT measurement was conducted with an ODT microscope (HT-2H, Tomocube, Daejeon, Korea) equipped with a 532 nm laser at 37°C in a humidified atmosphere containing 5% CO<sub>2</sub> [42-45]. In order to use as a reference for the ODT experiment, the RI value of the culture medium was measured through a refractometer (Abbemat 550; Anton Paar, Graz, Austria). The RI value of RPMI 1640 with 10% PBS is 1.3337 at 37°C. The RI values of the nucleolus, ER, and cytosol were calculated using TomoStudio software (ver. 2.6.25, Tomocube, Daejeon, Korea) following the manufacturer's protocol. Nanoparticles containing RITC were imaged in fluorescence 3D mode using an LED as the light source and an excitation filter of 575 $\pm$ 12 nm and an emission filter of 702 $\pm$ 98 nm. The RI value of ER was carried out with reference to the range using the ER-Tracker™ Blue-White DPX (Invitrogen, Oregon, USA). The sample is treated with an ER tracker at 1:2000 and then incubated at 37°C in a humidified atmosphere containing 5% CO<sub>2</sub> for 20 minutes. Thereafter, the ER tracker staining is confirmed by fluorescence. It was imaged in fluorescence 2D mode using an LED as the light source and an excitation filter of 392 $\pm$ 12 nm and an emission filter of 432 $\pm$ 18 nm.

## *2.6. Transmission electron microscopy (TEM)*

The morphology of the Si-FMNPs was characterized by transmission electron microscopy (TEM). The samples were dispersed in D.W and a drop of the suspension was placed on a copper grid (300 mesh, covered with carbon) followed by drying the grid at room temperature. TEM images were taken at 80 kV with a transmission electron microscope (Hitachi H-7600, Hitachi).

## *2.7. Dynamic Light Scattering (DLS) and Nanoparticle Tracking Analysis (NTA)*

For DLS and NTA measurement, each nanoparticle was made to have a volume of 1 ml in D.W. The ideal concentration of nanoparticles for measurement was found by pre-testing the ideal particle value per frame (20-50 particles per frame). Before the measurement, the samples were sonicated for 480s. DLS measurements were performed with a Litesizer 500 (Anton Paar, Graz, Austria) equipped with a 658nm laser. The software used for analyzing the data was Kalliope™. The hydrodynamic sizes and zeta potentials of the particle suspension were measured 5 runs of the 60s were performed with equilibration of the 60s at room temperature. The samples were performed using disposable cuvette (Sarstedt, Nümbrecht, Germany) for size measurement and Omega cuvette (Anton Paar, Graz, Austria) for zeta potential measurement. NTA measurements were carried out with a NanoSight NS300 (Malvern panalytical, Malvern, UK) equipped with a 488nm laser at 25°C, and analyzed using NTA software version 3.4. The hydrodynamic sizes and zeta potentials were carried out exactly like the DLS measurement. The sample was performed using disposable folded capillary cells (Malvern panalytical, Malvern, UK) for zeta potential measurement.

## 2.8. Cell Viability assay

The cell viability assay was carried out using Chromo-CK Cell Viability Assay KIT (Monobio, Seoul, Korea) and CellTiter-Glo® Luminescent Cell Viability Assay reagent (Promega, Wisconsin, USA) according to the manufacturer's instructions. Briefly, MCF7 cells were cultured ( $3.0 \times 10^3$  cells/well) into 96-well plates and incubated overnight at 37°C in a humidified atmosphere containing 5% CO<sub>2</sub>. The MCF7 cells were added with a solution of Si-FMNP (0.2mg/ml) for 0h, 5h, 10h, and 24h. In the case of Chromo-CK Cell Viability Assay KIT, the reagent (10  $\mu$ l/well) was treated to the 96-well (Nunc, NY, USA) and then incubated at 37°C in a humidified atmosphere containing 5% CO<sub>2</sub> for 1h. After incubation, absorbance was read at a wavelength of 450nm using Infinite M200 Pro (Tecan, Männedorf, Switzerland). In the case of Cell Titer-Glo, the reagent (20  $\mu$ l/well) was treated to the 96-well white plate (Corning, NY, USA) and then incubated at 37°C in a humidified atmosphere containing 5% CO<sub>2</sub> for 20 min. After incubation, luminescence was read using the Victor X3 Model 2030 Multilabel Plate Reader (Perkin Elmer, MA, USA).

## 3. Result

### *3.1. Characterization of the Si-FMNPs*

To evaluate the characteristic physical property of the Si-FMNPs with negative (Si-FMNP/OH) and positive (Si-FMNP/APTES) surface charges, ultrastructural morphology and diameter of the NPs were measured using transmission electron microscopy (TEM), dynamic light scattering (DLS), and nanoparticle tracking analysis (NTA) (**Fig. 1**). To evaluate the electrostatic properties, the zeta potential of the NPs was also measured. Representative TEM images of Si-FMNPs with negative and positive surface charges are shown in **Fig. 1a** and **b**, respectively. As shown in each figure, it can be seen that the case of nanoparticles having a circular shape and one magnetic core and the case having an elliptical shape and two magnetic cores are mixed. The elliptical nanoparticles including two magnetic cores are believed to be due to the formation of dimer nanoparticles during the synthesis process. The size distribution of individual Si-FMNPs was analyzed using image j software and showed normal distribution with an average diameter of 80.85nm for Si-FMNP/OH and 78.57nm for Si-FMNP/APTES, respectively (**Fig. 1c, d**). The EM analysis indicates that both nanoparticles were generally monodisperse and had a similar average diameter in a dry state. In addition, the hydrodynamic sizes of the two Si-FMNPs were measured in D.W by DLS and NTA and compared with the diameter obtained from TEM analysis as summarized in **Fig. 1e**. The hydrodynamic diameter of the nanoparticles obtained from DLS and NTA analysis was much larger than that obtained from TEM analysis. In previous studies, it has been reported that the hydrodynamic diameter of nanoparticles is larger than the particle size measured in the dry state [47-49]. The hydrodynamic diameter of the Si-FMNP/APTES was much higher than that of the Si-FMNP/OH. This difference may be due to the surface charge of the two nanoparticles in an aqueous solution or the difference in the degree of aggregation according to the APTES treatment (see also Materials and Methods). Average zeta potentials of Si-FMNP/OH and Si-

FMNP/APTES were measured to be -50mV and 20mV, respectively (**Fig. 1f**). This result suggests that the surface negative charge of Si-FMNP/OH nanoparticles was well substituted with positive charge through APTES treatment [50].

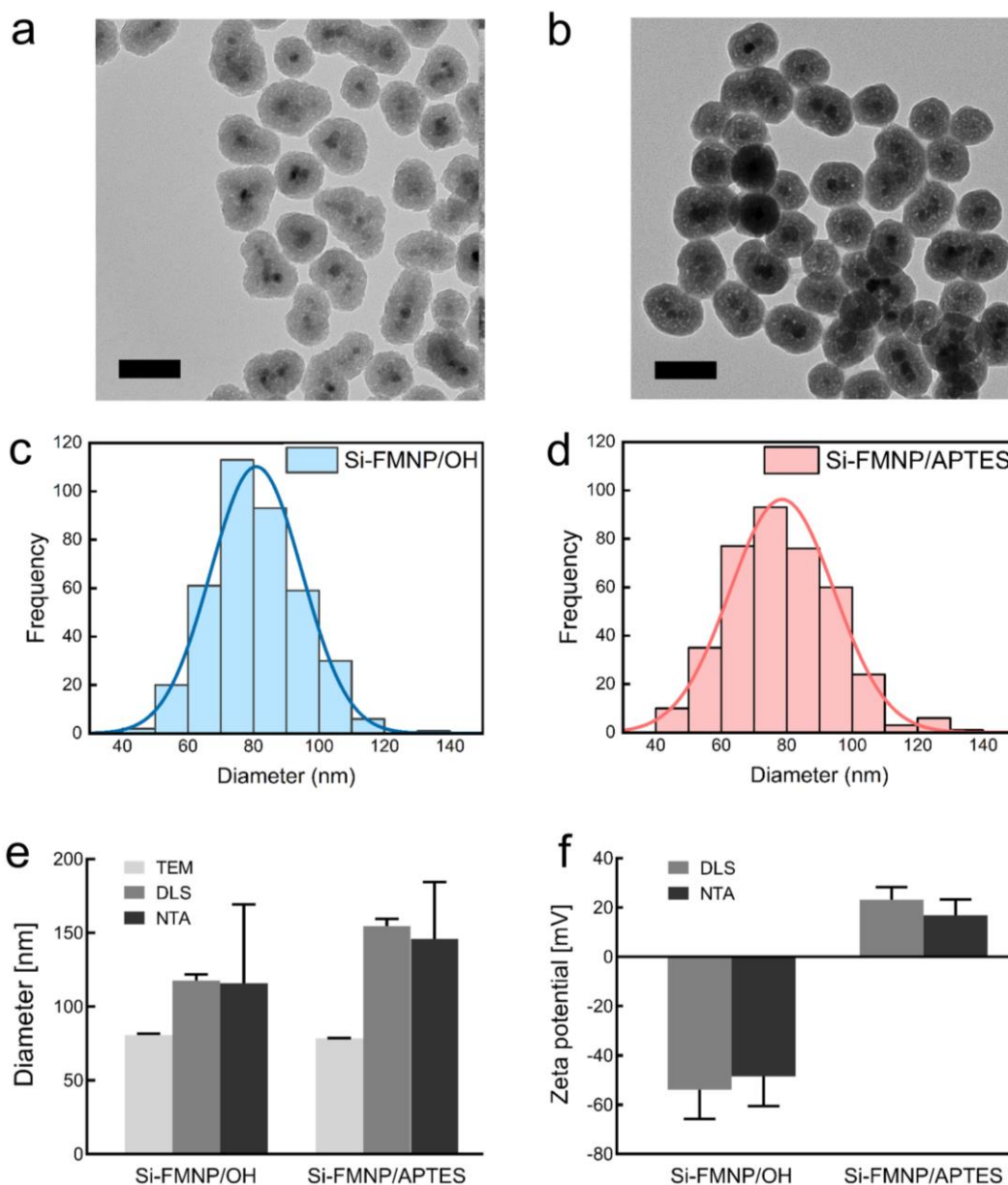


**Table 1.** Diameter, zeta potential of Si-FMNPs

NPs	Diameter (nm)			Zeta potential (mV)	
	TEM	DLS	NTA	DLS	NTA
Si-FMNP /OH	80.85±0.71	117.78±4.04	115.9±53.20	-53.9±11.90	-48.9±11.90
Si-FMNP /APTES	78.57±0.08	154.59±4.85	146.0±38.40	23.2±5.00	16.9±6.27

The diameter in TEM of the nanoparticles was evaluated in the dried state, whereas the hydrodynamic diameter of the nanoparticles was evaluated in the D.W.

### **Figure. 1 Characterization of the Si-FMNPs**

(a), (b) The TEM image of Si-FMNP/OH and Si-FMNP/APTES conjugated to RITC and the magnetic core in dry condition. Scale bar, 100nm. (c), (d) The size distribution of Si-FMNP/OH and Si-FMNP/APETS that was calculated by Image J software. n=385. (e) The size distribution from DLS, NTA, and TEM measurements of Si-FMNP/OH and Si-FMNP/APTES. Data are expressed as means $\pm$ SD. Error bars represent the standard deviation obtained from five measurements of the same sample. (f) The zeta potential from DLS and NTA measurements of Si-FMNP/OH and Si-FMNP/APTES. Data are expressed as means $\pm$ SEM. Error bars represent the standard error of the mean obtained from five measurements of the same sample.

### ***3.2. Effect of silica nanoparticles on cell viability***

In order to examine the cell toxicity of Si-FMNPs on MCF7 cells, cell viability was performed at 0h, 5h, 10h, and 24h after incubation with 0.2mg/ml concentration of Si-FMNPs. We cross-checked each experiment by performing two cell viability experiments with different evaluation methods. The 3-(4,5-dimethylthiazol-2-yl)-2,5-diphenyl-2H-tetrazolium bromide (MTT) assay evaluates cell viability using reducing activity as the enzymatic conversion of tetrazolium compounds to insoluble formazan crystals by dehydrogenase produced in the mitochondria of living cells [51,52]. However, metabolic activity can be altered by various conditions or drug treatments that can cause significant changes in the results described in the MTT assay [53, 54]. Because of this problem, high sensitivity assay was implemented as a method for measuring ATP. The luminescent cell viability assay is assessed by measuring the quantification of intracellular ATP following the luciferin-luciferase reaction in living cells. In living cells, the level of intracellular ATP remains constant, so the level of ATP in cells in culture is directly related to the number of living cells [55]. Because ATP is rapidly degraded in dead cells and decreased in damaged cells, it is highly sensitive, reproducible, and simple to assess cell viability and proliferation [56, 57]. As shown in **Fig. 2**, the viability of cells treated with Si-FMNP/OH decreased with time, but the viability of cells treated with Si-FMNP/APTES did not show any difference with time in MTT assay. However, the result of positively charged nanoparticles showed a different pattern from previous papers [12]. It suggests that the possibility of different toxicity depending on the cell line, the type of nanoparticles, and the concentration of nanoparticles. In the luminescence cell viability experiment, the viability of cells treated with Si-FMNP/OH was significantly reduced. In addition, the viability of cells treated with Si-FMNP/APTES was decreased at 24h. Based on the two experimental results, it was found that nanoparticles with different surface charges differed in terms of cytotoxicity. In particular, the cytotoxicity was conspicuously shown in the negatively charged nanoparticles.

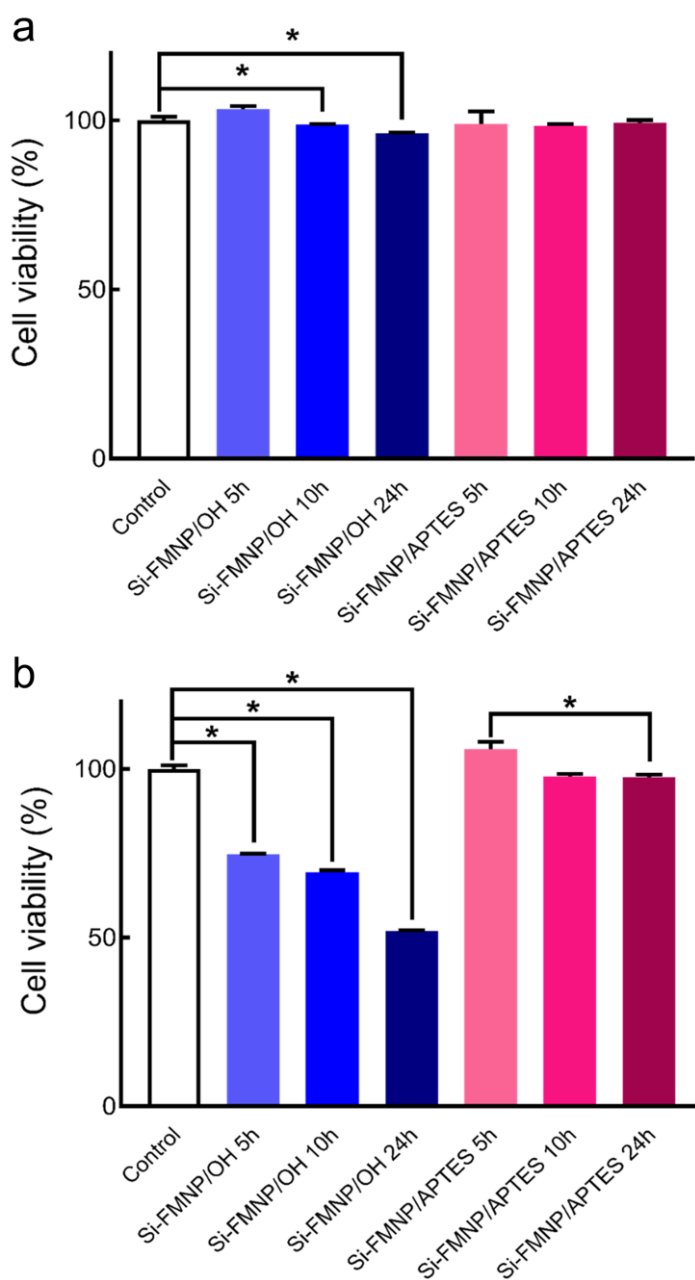
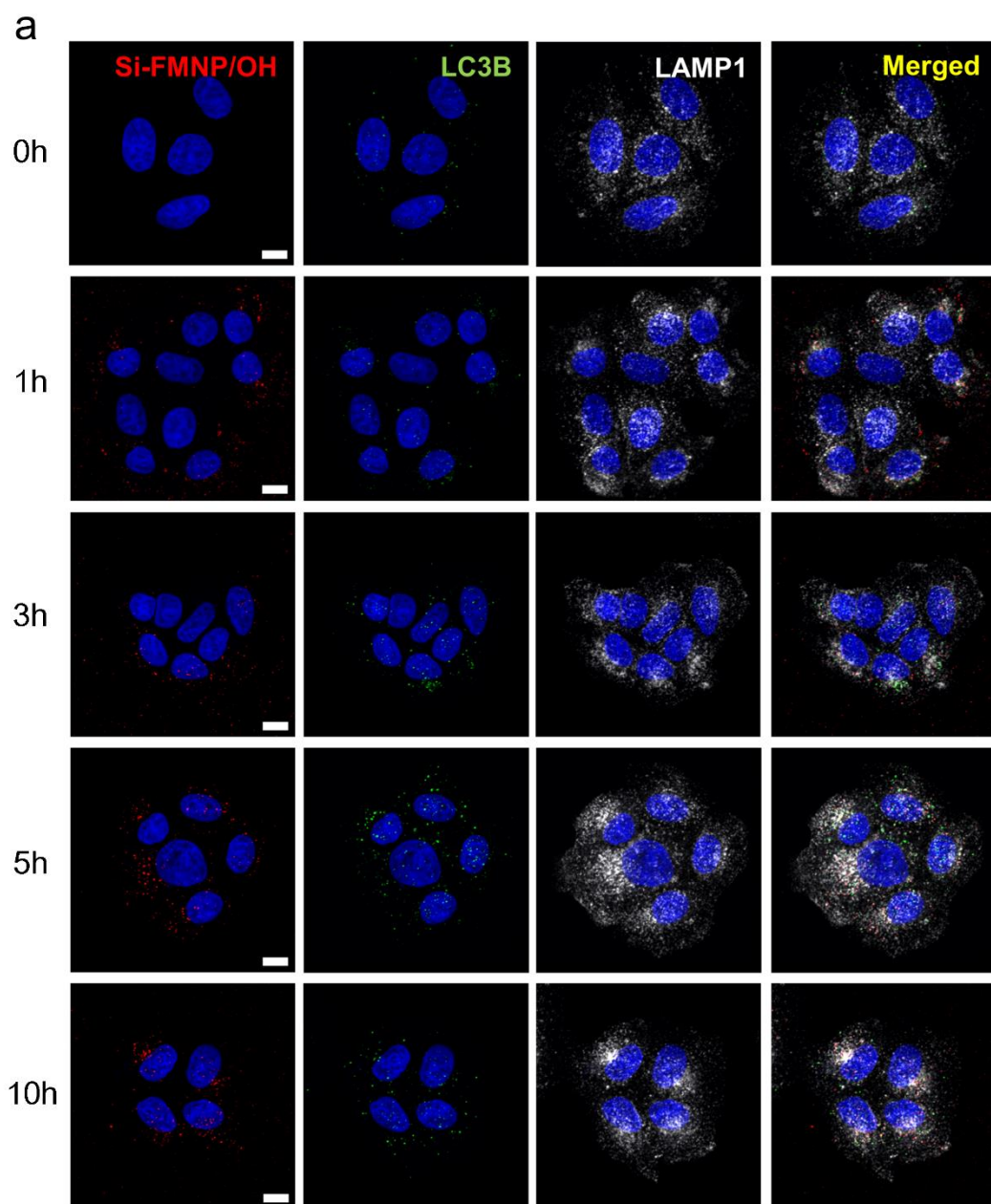


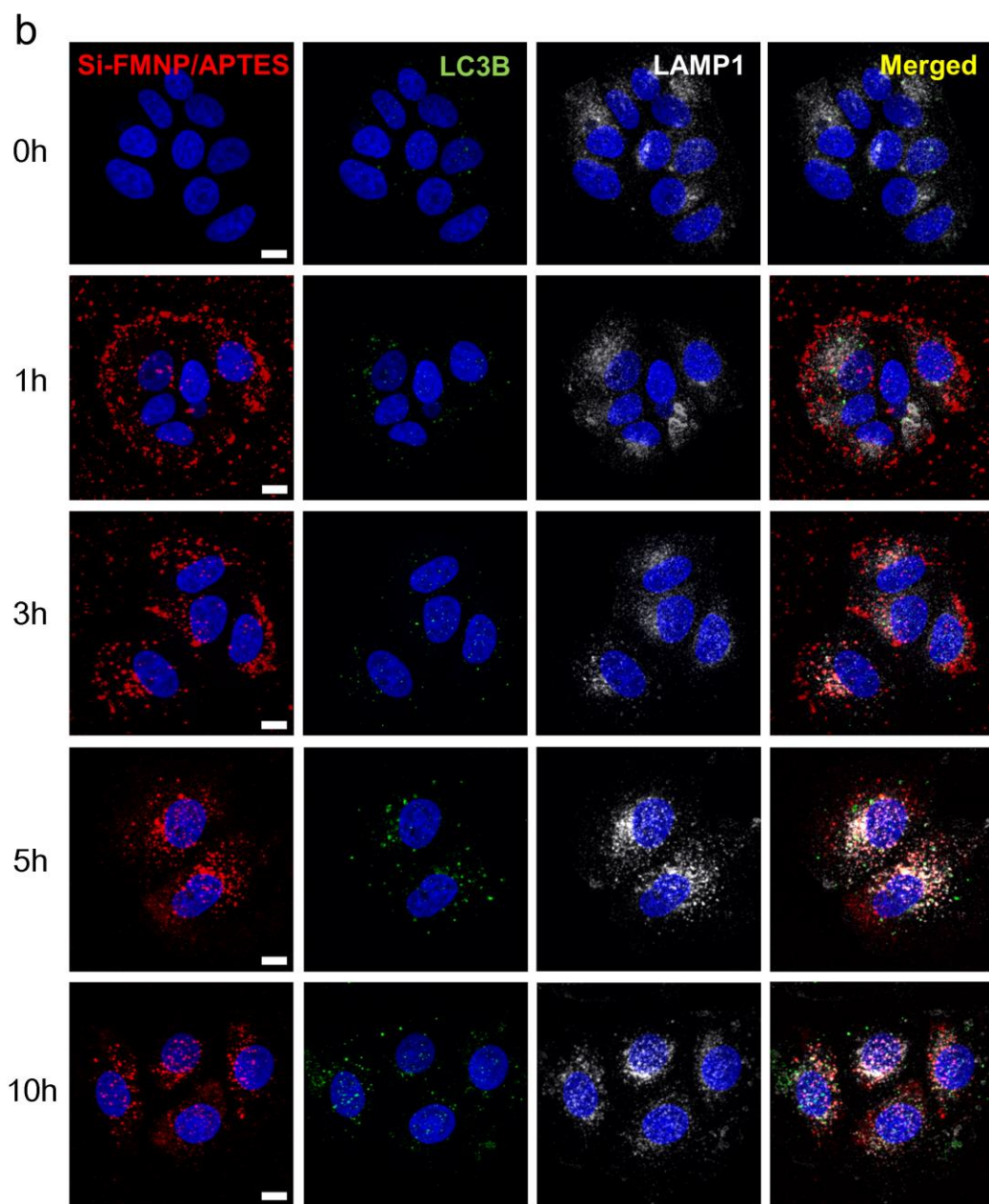
**Figure. 2 Effect of nanoparticles on cell viability in MCF7 cells**

Cell viability was performed at 0h, 5h, 10h, and 24h after incubation with 0.2mg/ml concentration of Si-FMNP/OH or Si-FMNP/APTES. Cell viability assays were conducted in MTT assay (**a**) and Luminescent cell viability assay (**b**), respectively. Data are expressed as means $\pm$ -SEM. Error bars represent the standard error of the mean obtained from three measurements of the same sample. \*  $p < 0.05$

### ***3.3. Quantitative analysis of autophagy induced by Si-FMNP/OH and Si-FMNP/APTES***

Since the spatio-temporal intracellular distribution of nanoparticles with different surface charges may play an important role in their biological effects, we experimented with the uptake of Si-FMNPs by MCF7 cells (**Fig. 3**). In the CLSM image, Si-FMNPs were distributed at the bottom of the dish and the edge of the cell at 1h and gradually moved to the cytoplasm and from the cytoplasm to the perinuclear region over time. In particular, it can be seen that there are a lot of both nanoparticles in the perinuclear region at 5h (**Fig.3a, 3b**). It is presumed that it was transported into cells through endocytosis [28]. It was known that the cell membrane is negative, so the positively charged nanoparticles could easily interact with the cell membrane [58]. Therefore, despite the treatment of the same concentration of nanoparticles, it was confirmed Si-FMNP/APTES was larger and internalized well into the cell. In order to confirm the interaction with organelles after Si-FMNPs treatment, immunofluorescence staining was conducted using autophagosome and lysosome marker protein. Each fluorescence intensity (F.I.) was obtained using the ZEN software for immunofluorescence-stained images (**Fig. 3c**). As seen in the CLSM image, the F.I. of Si-FMNP/APTES compared with Si-FMNP/OH was significantly different numerically. In the case of Si-FMNP/APTES, the F.I. gradually rose and peaked at 5h and then decreased, while F.I. of Si-FMNP/OH gradually increased and then became saturated from 5 hours. In the F.I. of LC3B, Si-FMNP/OH showed a decreasing trend up to 3 hours, then increased from 5 hours and reached a peak at 10 hours. The F.I. of LC3B of Si-FMNP/APTES was higher than that of Si-FMNP/OH at 1h. The F.I. value gradually increased, peaking at 5 hours and decreasing from 10 hours. Since the amount of LC3B is related to autophagosome [59], it indicates that the time point at which the nanoparticles induce autophagosome differed depending on the surface charge. The F.I. of LAMP1 showed a pattern similar to that of LC3B in both nanoparticles. As a result, it was confirmed that the dynamic properties of the overall process, including uptake and degradation, were different when Si-FMNPs with different surface charges were treated.





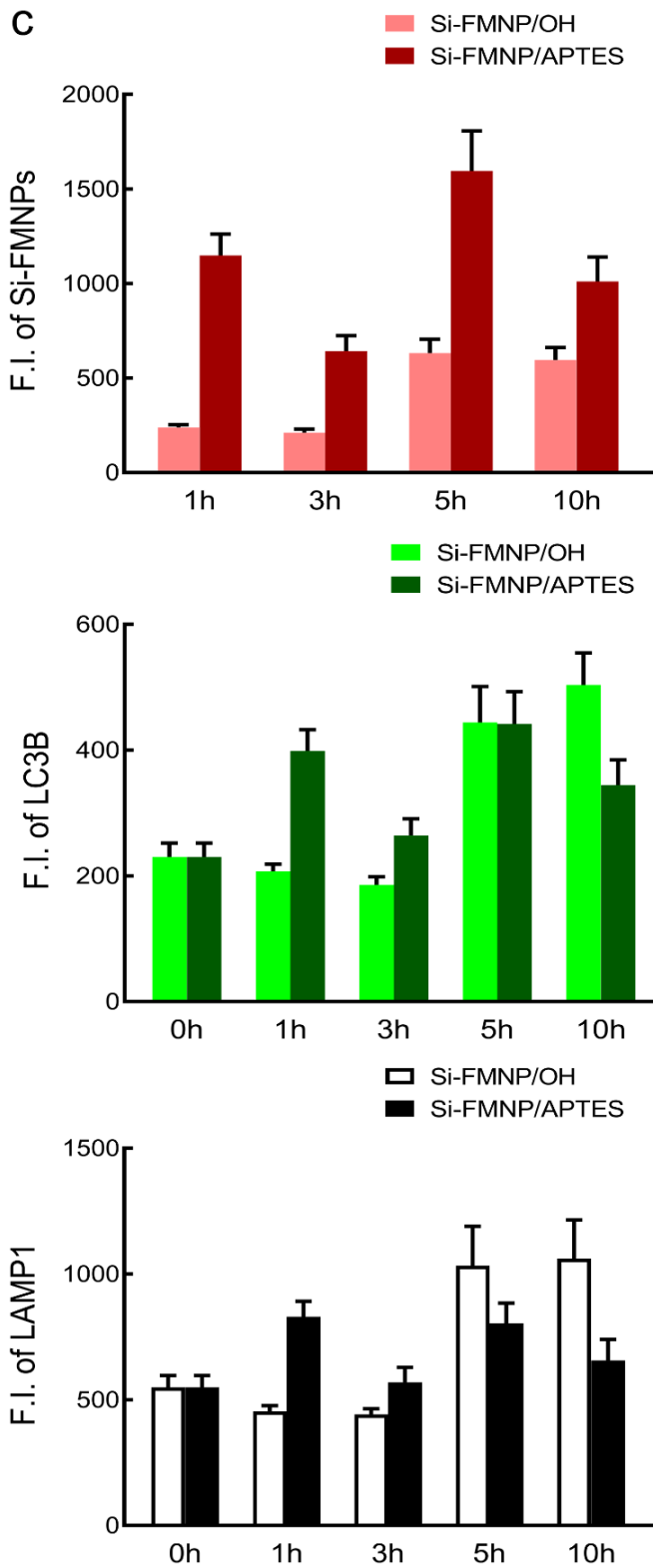


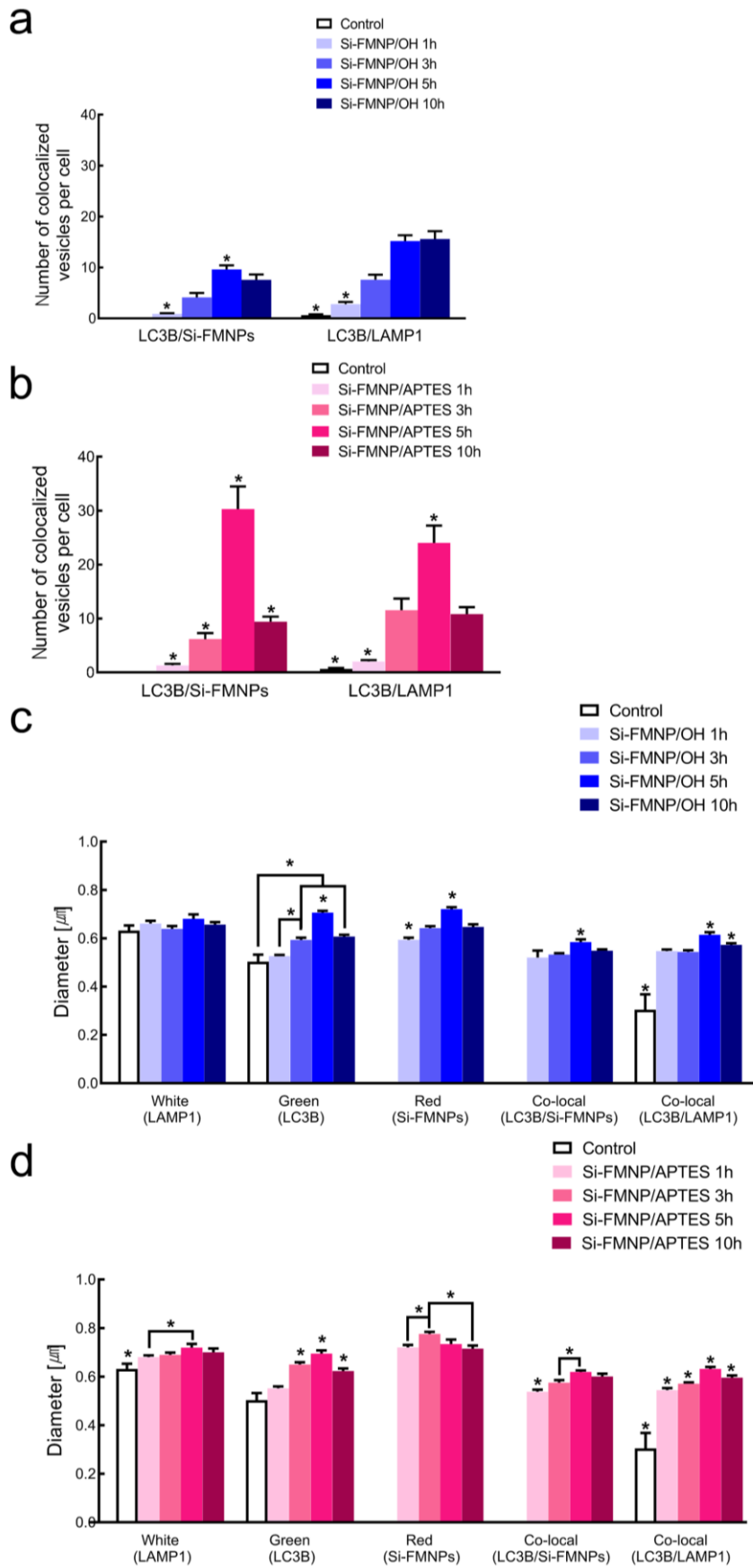
**Figure. 3 Immunofluorescence staining images of autophagy-induced MCF7 cells**

**(a,b)** Representative panels showed the images of Si-FMNP/OH (red), LC3B(green), LAMP1(white), and nuclei staining (DAPI, blue) of MCF7 cells treated with 0.2mg/ml of Si-FMNPs for 0h, 1h, 3h, 5h, and 10h. Scale bar, 10 $\mu$ m. **(c)** Immunofluorescence stained images were analyzed for each fluorescence intensity (F.I.) using ZEN software. The graphs in red, green, and white represent the mean F.I. of Si-FMNP, LC3B, and LAMP1, respectively. Data are expressed as means $\pm$ SEM (n=20).

The number of each fluorescent and colocalized vesicle was analyzed using IMARIS software (**Fig. 4a**). Here, considering the size of the endosome, autophagosome, and lysosome, the minimum diameter of each fluorescent vesicle was set to 0.5 $\mu$ m [60]. The colocalization of LC3B and Si-FMNPs increased with time, and then showed the highest peak at 5 hours, and then decreased after that. Considering Fig. 3c, these results of colocalization of Si-FMNPs are considered reasonable. In the case of Si-FMNP/OH, the colocalization of LAMP1 and LC3B gradually increased. On the other hand, in the case of Si-FMNP/APTES, the colocalization of LAMP1 and LC3B proceeded in a similar pattern to that of Si-FMNP/OH.

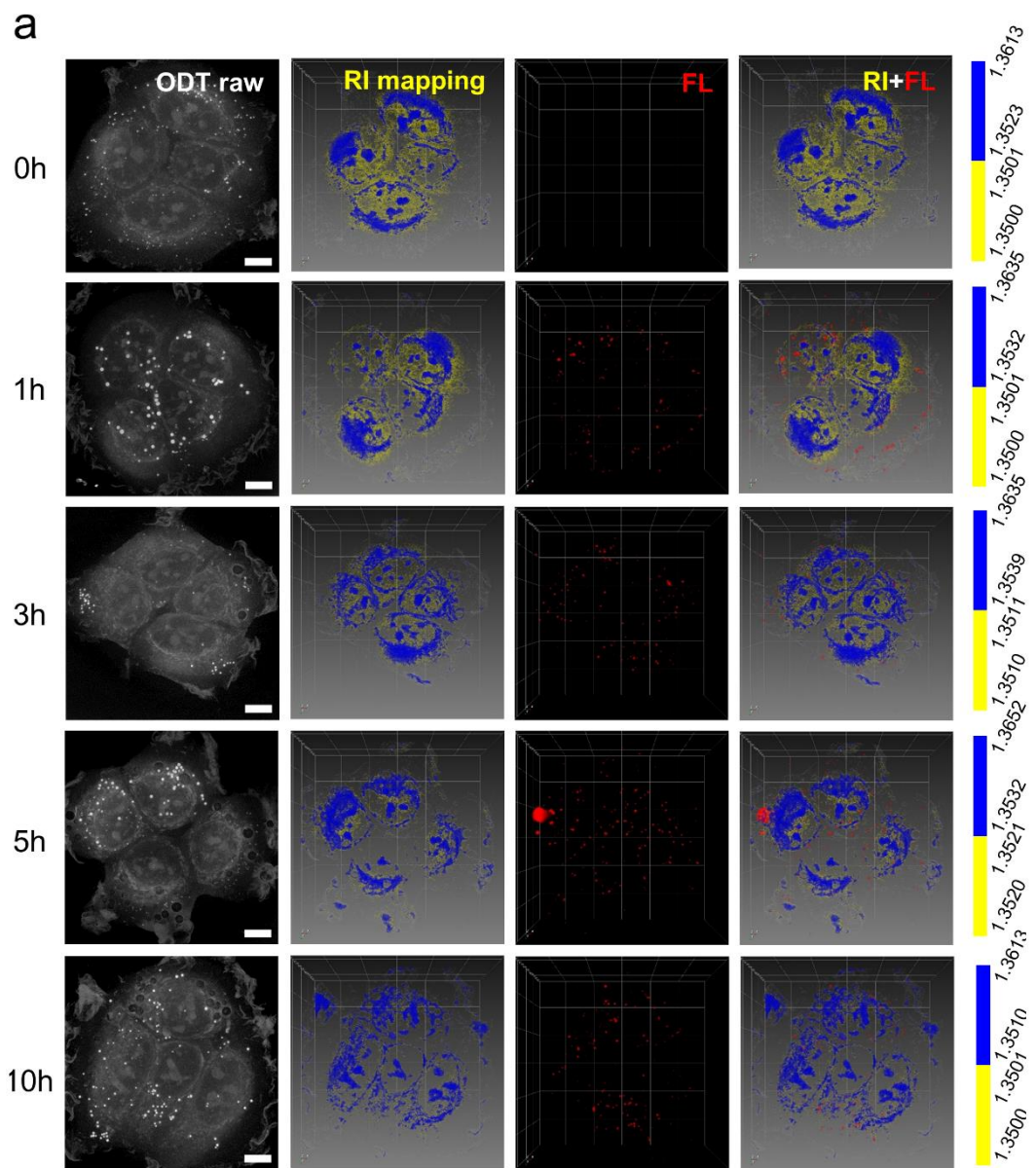
The diameter of the counted fluorescent vesicles could also be analyzed using the IMARS software (**Fig. 4b**). The diameters of LC3B and colocalization with LC3B and Si-FMNP/OH were high at 5h and decreased at 10 h. Considering the results of **Fig. 3b** and **Fig. 4a**, it seems that the number and size of autophagosomes including nanoparticle-induced autophagosome were large at 5h. However, at 10h, the size and number of autophagosomes are smaller than that of 5h. The number of LAMP1 and colocalization with LAMP1 and Si-FMNP/OH increases over time. The diameter colocalization with LAMP1 and Si-FMNP/OH changed significantly, but the value of LAMP1 did not. When Si-FMNP/APTES was treated, the diameter of LC3B and colocalization with LC3B and Si-FMNPs showed similar kinetic characteristics to that of Si-FMNP/OH. However, considering the results of **Fig. 3b** and **Fig. 4a**, it was found that autophagosomes including nanoparticle-induced autophagosomes were both large in size and number at 5 hours, and both decreased at 10 hours. In addition, the value of LAMP1 and colocalization with LAMP1 and Si-FMNP/APTES also decreased in size and number in the same way. This indicates to some extent consistent with the results of previous papers that NH<sub>2</sub>-polystyrene nanoparticles blocked autophagic flux by inducing lysosome dysfunction over time after induction of autophagy [33]. In the case of diameter and number of nanoparticles, Si-FMNP/OH was observed to be large at 5 hours, and Si-FMNP/APTES was observed to be the largest at 3 hours, and a large number was also observed at 5 hours.

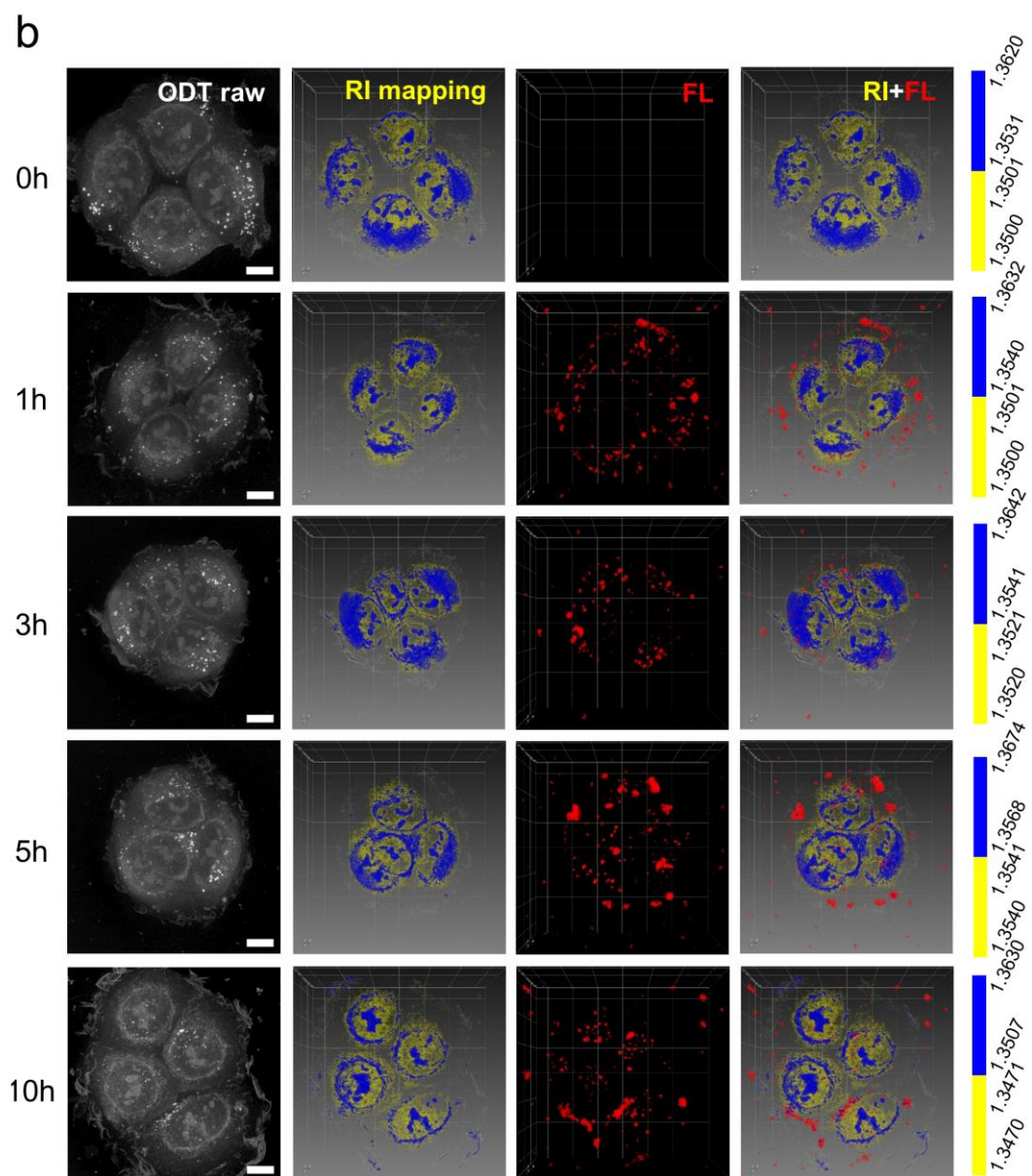
Looking at these results, it could be inferred that positively charged Si-FMNP/APTES, which are aggregated due to the characteristics of the electrostatic reactivity [61], have a larger diameter and are more internalized into the cell so that the autophagosomes were induced faster than the negatively charged Si-FMNP/OH.



**Figure. 4 Quantitative analysis of each fluorescent vesicles in the confocal image**

The number of each fluorescence in the immunofluorescent stained images was analyzed using IMARIS software. **(a), (b)** The result of calculating the colocalization of LC3B and Si-FMNP and LC3B and LAMP1 using the co-localization function of the IMARIS software. The minimum diameter of the counted fluorescent vesicles is  $0.5\mu\text{m}$ . The graph in blue color is the value for Si-FMNP/OH, and the graph in red color is for Si-FMNP/APTES. Data are expressed as means $\pm$ -SEM. (n=20). **(c), (d)** The diameter of the counted fluorescent vesicles was analyzed using the spot function of the IMARS software. The minimum diameter of the counted fluorescent vesicles is  $0.5\mu\text{m}$ . The graph in blue color is the value for Si-FMNP/OH, and the graph in red color is for Si-FMNP/APTES. Data are expressed as means $\pm$ -SEM (n=20),  
\*  $p < 0.05$





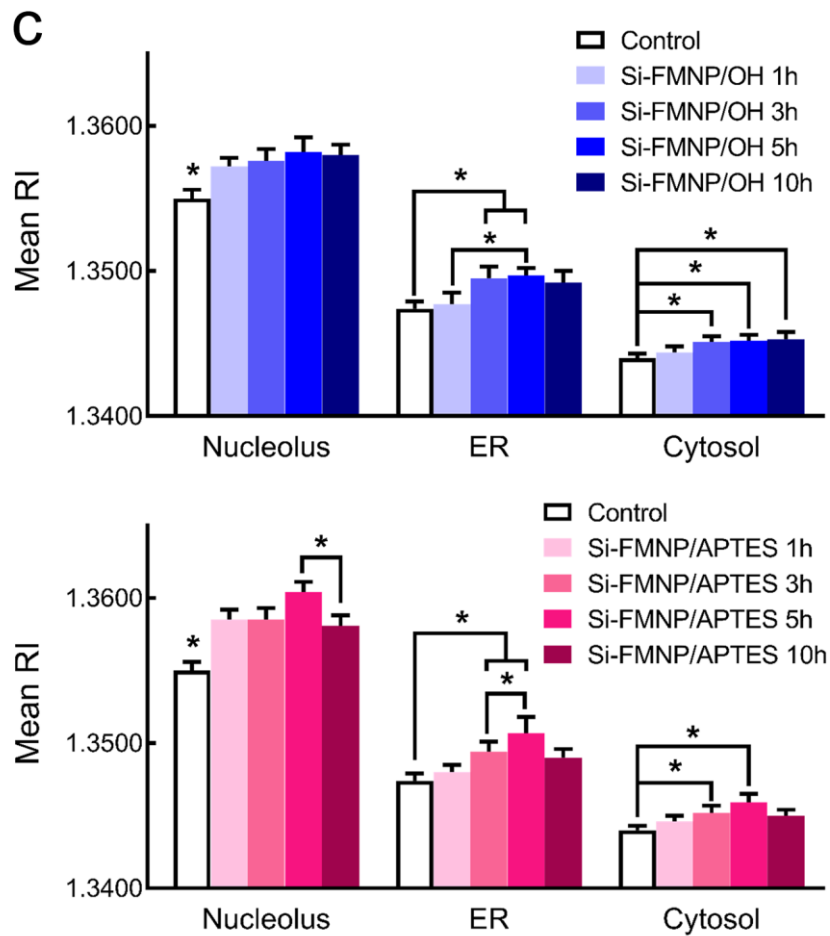


**Figure. 5 Spatio-temporal time change of the cellular RI values induced by Si-FMNPs**

(a), (b) Representative of raw ODT 3D images, pseudo-colored RI 3D images of the nucleolus(blue), endoplasmic reticulum(ER, yellow), and plasma membrane (white), the 2D fluorescent image of Si-FMNP(OH) (red), and merged image of RI 3D image and 2D fluorescent image. These are images obtained for each 0, 1, 3, 5, and 10 hours by treating MCF7 cells with Si-FMNP/OH or Si-FMNP/APTES at a concentration of 0.2 mg/ml. Scale bar, 10 $\mu$ m. (c) Mean values of refractive index (RI) of the nucleolus, ER, and cytosol. Data are expressed as means $\pm$ SEM (n=10) \*  $p < 0.05$ .

**Table 2.** Mean refractive index (RI) of cellular organelles

<b>Si-FMNP/APTES treatment time</b>	<b>Nucleolus</b>	<b>ER</b>	<b>Cytosol</b>	<b>Plasma membrane</b>
0h	1.3550±0.0006	1.3474±0.0005	1.3440±0.0003	1.3379±0
1h	1.3585±0.0007	1.3480±0.0005	1.3446±0.0004	1.3379±0
3h	1.3585±0.0008	1.3494±0.0007	1.3452±0.0005	1.3379±0
5h	1.3604±0.0007	1.3507±0.0011	1.3459±0.0006	1.3379±0
10h	1.3581±0.0007	1.3490±0.0008	1.3450±0.0004	1.3379±0

<b>Si-FMNP/OH treatment time</b>	<b>Nucleolus</b>	<b>ER</b>	<b>Cytosol</b>	<b>Plasma membrane</b>
0h	1.3550±0.0006	1.3474±0.0005	1.3440±0.0003	1.3379±0
1h	1.3572±0.0006	1.3477±0.0008	1.3444±0.0004	1.3379±0
3h	1.3576±0.0008	1.3495±0.0008	1.3451±0.0004	1.3379±0
5h	1.3582±0.0010	1.3497±0.0005	1.3452±0.0004	1.3379±0
10h	1.3580±0.0007	1.3492±0.0008	1.3453±0.0005	1.3379±0

There are 4 significant figures after the decimal point.

### ***3.4. Spatio-temporal change of the cellular RI values induced by Si-FMNPs***

To investigate the physical effect of Si-FMNPs treatment on organelles such as cytoplasm, cytosol, nucleolus, and endoplasmic reticulum (ER), the intracellular distribution of Si-FMNPs and the refractive index (RI) of organelles were quantitatively analyzed using a label-free 3D optical diffraction tomography (ODT) (**Fig. 5**). A single living cell is a complex structure containing numerous organelles with different RI. The RI values vary as the relative abundance of different organelles, cell/nuclear size, protein content, etc. vary from cell to cell [62]. Since the nucleolus has the highest molecular density in the nucleus, the brightest element in the nucleus is assumed to be the nucleolus and expressed as a pseudo-color of blue. The RI mapping, set in pseudo-color of blue, included regions of the nucleolus, nuclear membrane, and dense ER. In addition, RI mapping with a yellow pseudo-color was performed to express the ER region. The boundary of the ER region was performed using an ER tracker (**Fig.S3**). After Si-FMNP/OH treatment, it was confirmed that the RI mapping region expressed in blue pseudo color gradually widened and overlapped with the RI mapping of yellow pseudo-color (**Fig.5a**). On the other hand, in the case of Si-FMNP/APTES treatment, it was confirmed that the RI mapping expressed in blue pseudo-color was widened up to 3 hours treatment, but gradually decreased after 5 hours (**Fig.5b**). In the fluorescence images, it was confirmed that the nanoparticles migrated from the cell membrane to the cytoplasm and from the cytoplasm to the perinuclear part over time. Also, it was confirmed that Si-FMNP/APTES was uptaken more than Si-FMNP/OH despite treatment with the same concentration. It seems the same pattern as the immunofluorescence staining image (**Fig 3**).

When both nanoparticles were treated, the RI values of the nucleolus significantly increased over time compared to the control group (**Fig. 5c**). It suggests that since nucleolus is an organelle related to cellular stress, many substances were synthesized to prepare for stress in a situation where nanoparticles, which are foreign substances, were treated [64-66]. Also, the

RI values of ER and cytosol tended to increase. This is presumed to be affected by the accumulation in the perinuclear regions due to endocytosis of Si-FMNPs. Considering the tendency, the RI values in the Si-FMNP/OH-treated experiment showed a tendency to saturation with time. On the other hand, in the Si-FMNP/APTES-treated experiment, the RI values increased compared to the control group, and then showed the highest value at 5 hours, and then decreased. In addition, the RI value of the group treated with Si-FMNP/APTES was higher than that of the group treated with Si-FMNP/OH. The difference in the tendency to change the refractive index of organelles depending on the surface charge despite the treatment with the same concentration of nanoparticles suggests that this is an essential consideration for drug delivery development.

## 4. Discussion

This study was investigated the spatiotemporal subcellular distribution and organelle interactions of Si-FMNPs with different surface charges. It found that positively charged nanoparticles were more significantly uptaken into cells than negatively charged nanoparticles (**Fig. 3**), which is consistent with previous studies [12, 15]. Additionally, it demonstrated that Si-FMNPs induce autophagy by increasing the value of F.I. of LC3B and LAMP1 (**Fig. 3**). In a previous study, each nanoparticle of MEF cells was treated using a confocal fluorescence microscope and co-localization was confirmed using a lysotracker [33]. This study demonstrated the kinetic characteristics of the entire process including autophagosomes as well as quantitative analysis of each fluorescence and uptake and degradation of nanoparticle (**Fig. 4**). There are notable differences in the quantitative analysis as well as the images of autophagosomes overtime themselves. After Si-FMNPs treatment, colocalization was confirmed in both nanoparticles, but positively charged particles were quantitatively higher than negatively charged particles. Furthermore, the kinetics of autophagy and degradation processes were significantly different despite the same concentration of nanoparticles. As the kinetic properties of autophagy and degradation processes depend on the surface charge of nanoparticles, this is presumably related to the cell toxicity related to cell viability (**Fig. 2**).

Using the non-invasive ODT technique, the accumulation pattern of Si-FMNPs in living cells from the cell membrane to the cytoplasm over time and from the cytoplasm to the perinuclear region (**Fig. 5**) was consistent with the pattern shown in the immunofluorescence staining images (**Fig. 3**). Previous studies have shown that the RI values of whole cells are increased after nanoparticle treatment [66, 67]. Meanwhile, this study demonstrated that the RI of the nucleolus, ER, and cytoplasm increased compared to the control by quantitatively analyzing the RI change of each organelle, not the total cellular RI value after nanoparticle treatment. In addition, it was confirmed that the RI values of kinetic properties of each

organelle according to the processing time depended on the surface charge of the nanoparticles.

This study showed that the surface charge should be considered as an important factor to be considered when designing a drug carrier in a drug delivery system. In addition, if such ODT technology is used, it will be possible to observe absorption into cells without fluorescence by treating nanoparticles with fluorescence in this study, but nanoparticles or exosomes have a high refractive index. At the single-cell level, it seems possible to quantitatively evaluate the therapeutic effects of nanomedicine through real-time monitoring of the three-dimensional dynamics that affect the targeted delivery of cells. This provides new insights as a method to evaluate drug carriers in drug delivery systems.

## 5. Conclusion

It was demonstrated that positively charged nanoparticles were uptaken into the cell more than negatively charged nanoparticles. These results suggest that the surface charge is an important factor in determining intracellular uptake efficiency. This study also performed a quantitative analysis of the interaction between nanoparticles and organelles within cells utilizing imaging techniques such as fluorescence immunostaining and ODT. Strikingly, it was found that the kinetic characteristics of autophagy and degradation processes depend on the surface charge of the nanoparticles. In particular, label-free 3D ODT technology is likely to be evaluated as a promising technology for quantitative evaluation by monitoring the effects of nanoparticles (i.e nano-carrier containing drug) on cells in real-time at the single-cell level. Consequently, this study, for the first time, demonstrates the different processes after intracellular uptake of two Si-FMNPs with different surface charges, such as spatio-temporal distribution and interactions with organelles, especially autophagosome, and cell toxicity. Our study is expected to greatly contribute to the design and development of more effective and safe nano-carrier.

## 6. References

1. Moghimi, S.M., A.C. Hunter, and J.C. Murray, Nanomedicine: current status and future prospects. *Faseb j*, 2005. 19(3): p. 311-30.
2. Mora-Huertas, C.E., H. Fessi, and A. Elaissari, Polymer-based nanocapsules for drug delivery. *Int J Pharm*, 2010. 385(1-2): p. 113-42.
3. Wagner, V., et al., The emerging nanomedicine landscape. *Nat Biotechnol*, 2006. 24(10): p. 1211-7.
4. Papavlassopoulos, H., et al., Toxicity of functional nano-micro zinc oxide tetrapods: impact of cell culture conditions, cellular age and material properties. *PLoS One*, 2014. 9(1): p. e84983.
5. Mishra, Y.K. and R. Adelung, ZnO tetrapod materials for functional applications. *Materials Today*, 2018. 21(6): p. 631-651.
6. Kou, L., et al., Transporter-Guided Delivery of Nanoparticles to Improve Drug Permeation across Cellular Barriers and Drug Exposure to Selective Cell Types. *Frontiers in Pharmacology*, 2018. 9(27).
7. Sumer, B. and J. Gao, Theranostic nanomedicine for cancer. *Nanomedicine (Lond)*, 2008. 3(2): p. 137-40.
8. Behzadi, S., et al., Cellular uptake of nanoparticles: journey inside the cell. *Chem Soc Rev*, 2017. 46(14): p. 4218-4244.
9. Ulbrich, K., et al., Targeted Drug Delivery with Polymers and Magnetic Nanoparticles: Covalent and Noncovalent Approaches, Release Control, and Clinical Studies. *Chemical Reviews*, 2016. 116(9): p. 5338-5431.

10. Blanco, E., H. Shen, and M. Ferrari, Principles of nanoparticle design for overcoming biological barriers to drug delivery. *Nature Biotechnology*, 2015. 33(9): p. 941-951.
11. Wilhelm, S., et al., Analysis of nanoparticle delivery to tumours. *Nature Reviews Materials*, 2016. 1(5): p. 16014.
12. Jeon, S., et al., Surface Charge-Dependent Cellular Uptake of Polystyrene Nanoparticles. *Nanomaterials (Basel)*, 2018. 8(12).
13. Kinnear, C., et al., Form Follows Function: Nanoparticle Shape and Its Implications for Nanomedicine. *Chemical Reviews*, 2017. 117(17): p. 11476-11521.
14. Gattoo, M.A., et al., Physicochemical Properties of Nanomaterials: Implication in Associated Toxic Manifestations. *BioMed Research International*, 2014. 2014: p. 498420.
15. Osaka, T., et al., Effect of surface charge of magnetite nanoparticles on their internalization into breast cancer and umbilical vein endothelial cells. *Colloids and Surfaces B: Biointerfaces*, 2009. 71(2): p. 325-330.
16. Stöber, W., A. Fink, and E. Bohn, Controlled growth of monodisperse silica spheres in the micron size range. *Journal of Colloid and Interface Science*, 1968. 26(1): p. 62-69.
17. Sailor, M.J. and J.H. Park, Hybrid nanoparticles for detection and treatment of cancer. *Adv Mater*, 2012. 24(28): p. 3779-802.
18. Radu, D.R., et al., A Polyamidoamine Dendrimer-Capped Mesoporous Silica Nanosphere-Based Gene Transfection Reagent. *Journal of the American Chemical Society*, 2004. 126(41): p. 13216-13217.
19. Ruedas-Rama, M.J., et al., Fluorescent nanoparticles for intracellular sensing: A review. *Analytica Chimica Acta*, 2012. 751: p. 1-23.

20. Chitra, K. and G. Annadurai, Rapid capture and exemplary detection of clinical pathogen using surface modified fluorescent silica coated iron oxide nanoparticles. *Biocybernetics and Biomedical Engineering*, 2014. 34(4): p. 230-237.
21. Wan, J., et al., Incorporation of magnetite nanoparticle clusters in fluorescent silica nanoparticles for high-performance brain tumor delineation. *Nanotechnology*, 2010. 21(23): p. 235104.
22. Cho, Y.-S., et al., Cetuximab-conjugated magneto-fluorescent silica nanoparticles for in vivo colon cancer targeting and imaging. *Cancer Letters*, 2010. 299(1): p. 63-71.
23. Arap, W., et al., Luminescent silica nanoparticles for cancer diagnosis. *Curr Med Chem*, 2013. 20(17): p. 2195-211.
24. Jeelani, P.G., et al., Multifaceted Application of Silica Nanoparticles. A Review. *Silicon*, 2020. 12(6): p. 1337-1354.
25. Castillo, R.R., M. Colilla, and M. Vallet-Regí, Advances in mesoporous silica-based nanocarriers for co-delivery and combination therapy against cancer. *Expert Opin Drug Deliv*, 2017. 14(2): p. 229-243.
26. Lucht, N., et al., Biophysical Characterization of (Silica-coated) Cobalt Ferrite Nanoparticles for Hyperthermia Treatment. *Nanomaterials (Basel)*, 2019. 9(12).
27. Aşık, E., et al., Cellular uptake, genotoxicity and cytotoxicity of cobalt ferrite magnetic nanoparticles in human breast cells. *Toxicol Res (Camb)*, 2016. 5(6): p. 1649-1662.
28. Tada, D.B., et al., Methylene Blue-Containing Silica-Coated Magnetic Particles: A Potential Magnetic Carrier for Photodynamic Therapy. *Langmuir*, 2007. 23(15): p. 8194-8199.

29. Zhang, S., H. Gao, and G. Bao, Physical Principles of Nanoparticle Cellular Endocytosis. *ACS Nano*, 2015. 9(9): p. 8655-8671.
30. Mishra, A.R., et al., Silver Nanoparticle-Induced Autophagic-Lysosomal Disruption and NLRP3-Inflammasome Activation in HepG2 Cells Is Size-Dependent. *Toxicol Sci*, 2016. 150(2): p. 473-87.
31. Ma, X., et al., Gold nanoparticles induce autophagosome accumulation through size-dependent nanoparticle uptake and lysosome impairment. *ACS Nano*, 2011. 5(11): p. 8629-39.
32. Zhao, Y., et al., Exposure to titanium dioxide nanoparticles induces autophagy in primary human keratinocytes. *Small*, 2013. 9(3): p. 387-92.
33. Wang, F., A. Salvati, and P. Boya, Lysosome-dependent cell death and deregulated autophagy induced by amine-modified polystyrene nanoparticles. *Open Biol*, 2018. 8(4).
34. Wei, F., et al., New findings of silica nanoparticles induced ER autophagy in human colon cancer cell. *Sci Rep*, 2017. 7: p. 42591.
35. Klionsky, D.J., Autophagy: from phenomenology to molecular understanding in less than a decade. *Nature Reviews Molecular Cell Biology*, 2007. 8(11): p. 931-937.
36. Glick, D., S. Barth, and K.F. Macleod, Autophagy: cellular and molecular mechanisms. *J Pathol*, 2010. 221(1): p. 3-12.
37. Choi, W., et al., Tomographic phase microscopy. *Nature Methods*, 2007. 4(9): p. 717-719.
38. Turko, N.A., A. Peled, and N.T. Shaked, Wide-field interferometric phase microscopy with molecular specificity using plasmonic nanoparticles. *J Biomed Opt*, 2013. 18(11): p. 111414.

39. Kim, K., et al., High-resolution three-dimensional imaging of red blood cells parasitized by Plasmodium falciparum and in situ hemozoin crystals using optical diffraction tomography. *J Biomed Opt*, 2014. 19(1): p. 011005.
40. Kim, K., et al., Real-time visualization of 3-D dynamic microscopic objects using optical diffraction tomography. *Optics Express*, 2013. 21(26): p. 32269-32278.
41. Kim, K., J. Yoon, and Y. Park, Simultaneous 3D visualization and position tracking of optically trapped particles using optical diffraction tomography. *Optica*, 2015. 2(4): p. 343-346.
42. Kim, T.K., et al., Physicochemical Properties of Nucleoli in Live Cells Analyzed by Label-Free Optical Diffraction Tomography. *Cells*, 2019. 8(7).
43. Park, Y., et al., Static and dynamic light scattering of healthy and malaria-parasite invaded red blood cells. *J Biomed Opt*, 2010. 15(2): p. 020506.
44. Kim, Y.S., et al., Combining Three-Dimensional Quantitative Phase Imaging and Fluorescence Microscopy for the Study of Cell Pathophysiology. *Yale J Biol Med*, 2018. 91(3): p. 267-277.
45. Jung, J., et al., Hyperspectral optical diffraction tomography. *Optics Express*, 2016. 24(3): p. 2006-2012.
46. Kim, T.K., et al., Mitotic Chromosomes in Live Cells Characterized Using High-Speed and Label-Free Optical Diffraction Tomography. *Cells*, 2019. 8(11).
47. Pack, C.G., et al., Microenvironments and different nanoparticle dynamics in living cells revealed by a standard nanoparticle. *J Control Release*, 2012. 163(3): p. 315-21.

48. Souza, T.G.F., V.S.T. Ciminelli, and N.D.S. Mohallem, A comparison of TEM and DLS methods to characterize size distribution of ceramic nanoparticles. *Journal of Physics: Conference Series*, 2016. 733: p. 012039.
49. Kaasalainen, M., et al., Size, Stability, and Porosity of Mesoporous Nanoparticles Characterized with Light Scattering. *Nanoscale Research Letters*, 2017. 12(1): p. 74.
50. Hosseini, F., M. Seyedsadjadi, and N. Farhadyar, Fe<sub>3</sub>O<sub>4</sub> nanoparticles modified with APTES as the carrier for (+)-(S)-2-(6-methoxynaphthalen-2-yl) propanoic acid (Naproxen) and (RS) 2-(3-benzoylphenyl)-propionic acid (Ketoprofen) drug. *Oriental journal of chemistry*, 2014. 30: p. 1609-1618.
51. Lü, L., et al., Exocytosis of MTT formazan could exacerbate cell injury. *Toxicol In Vitro*, 2012. 26(4): p. 636-44.
52. Stockert, J.C., et al., MTT assay for cell viability: Intracellular localization of the formazan product is in lipid droplets. *Acta Histochem*, 2012. 114(8): p. 785-96.
53. Plumb, J.A., R. Milroy, and S.B. Kaye, Effects of the pH dependence of 3-(4,5-dimethylthiazol-2-yl)-2,5-diphenyl-tetrazolium bromide-formazan absorption on chemosensitivity determined by a novel tetrazolium-based assay. *Cancer Res*, 1989. 49(16): p. 4435-40.
54. Hsu, S., et al., Green tea polyphenols induce differentiation and proliferation in epidermal keratinocytes. *J Pharmacol Exp Ther*, 2003. 306(1): p. 29-34.
55. Morciano, G., et al., Use of luciferase probes to measure ATP in living cells and animals. *Nature Protocols*, 2017. 12(8): p. 1542-1562.
56. Crouch, S.P., et al., The use of ATP bioluminescence as a measure of cell proliferation and cytotoxicity. *J Immunol Methods*, 1993. 160(1): p. 81-8.

57. Kangas, L., M. Grönroos, and A.L. Nieminen, Bioluminescence of cellular ATP: a new method for evaluating cytotoxic agents in vitro. *Med Biol*, 1984. 62(6): p. 338-43.
58. Chung, T.-H., et al., The effect of surface charge on the uptake and biological function of mesoporous silica nanoparticles in 3T3-L1 cells and human mesenchymal stem cells. *Biomaterials*, 2007. 28(19): p. 2959-2966.
59. Mizushima, N. and T. Yoshimori, How to Interpret LC3 Immunoblotting. *Autophagy*, 2007. 3(6): p. 542-545.
60. Yim, W.W.-Y. and N. Mizushima, Lysosome biology in autophagy. *Cell Discovery*, 2020. 6(1): p. 6.
61. Ishiwata, H., et al., Characteristics and biodistribution of cationic liposomes and their DNA complexes. *J Control Release*, 2000. 69(1): p. 139-48.
62. Gul, B., et al., Cell refractive index: Models, insights, applications and future perspectives. *Photodiagnosis and Photodynamic Therapy*, 2021. 33: p. 102096.
63. Mangan, H., M. Gailín, and B. McStay, Integrating the genomic architecture of human nucleolar organizer regions with the biophysical properties of nucleoli. *Febs j*, 2017. 284(23): p. 3977-3985.
64. Boulon, S., et al., The nucleolus under stress. *Mol Cell*, 2010. 40(2): p. 216-27.
65. Pfister, A.S., Emerging Role of the Nucleolar Stress Response in Autophagy. *Frontiers in Cellular Neuroscience*, 2019. 13(156).
66. Kim, D., et al., Label-free high-resolution 3-D imaging of gold nanoparticles inside live cells using optical diffraction tomography. *Methods*, 2018. 136: p. 160-167.

67. Park, S., et al., Label-Free Tomographic Imaging of Lipid Droplets in Foam Cells for Machine-Learning-Assisted Therapeutic Evaluation of Targeted Nanodrugs. *ACS Nano*, 2020. 14(2): p. 1856-1865.

## 7. Supplementary data

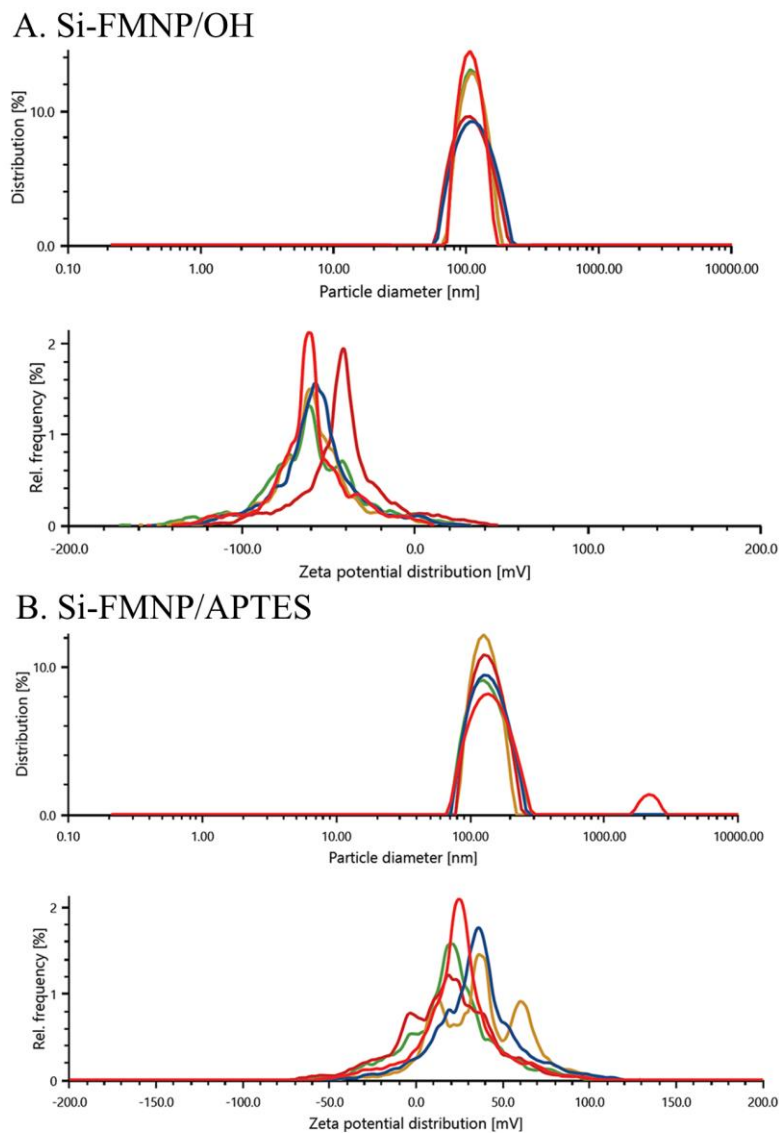
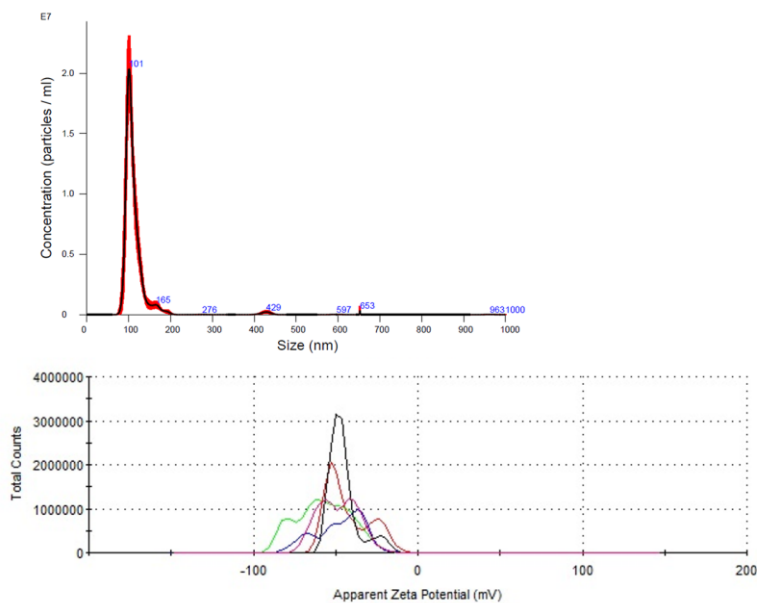


**Fig S1. Distribution of diameter and zeta potential of nanoparticles measured by dynamic light scattering (DLS)**

(A) Representative raw data of size and zeta potential distribution of Si-FMNP/OH. (B) Raw data of size and zeta potential distribution of Si-FMNP/APTES. The measurement was repeated 5 times and a normal distribution was achieved.

### A. Si-FMNP/OH



### B. Si-FMNP/APTES

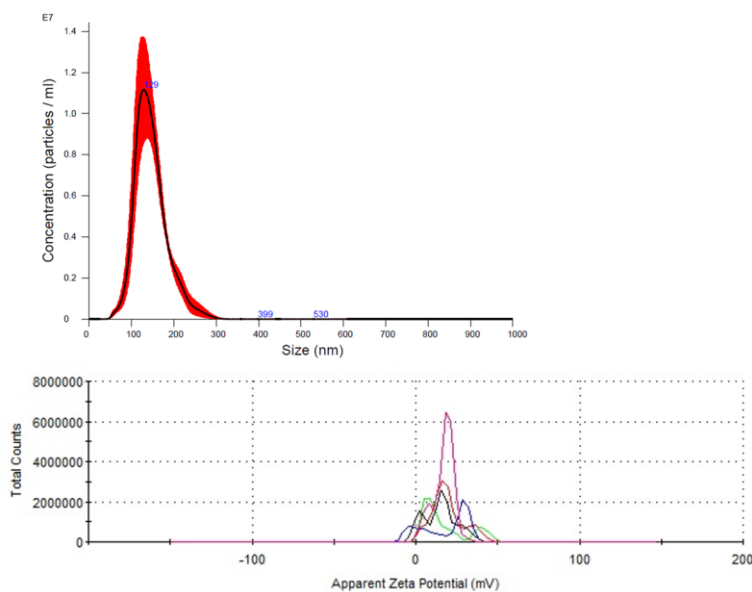


**Fig S2. Distribution of diameter and zeta potential of nanoparticles measured by Nanoparticle Tracking Analysis (NTA)**

(A) Representative raw data of size and zeta potential distribution of Si-FMNP/OH. (B) Raw data of size and zeta potential distribution of Si-FMNP/APTES. The measurement was repeated 5 times and a normal distribution was achieved.

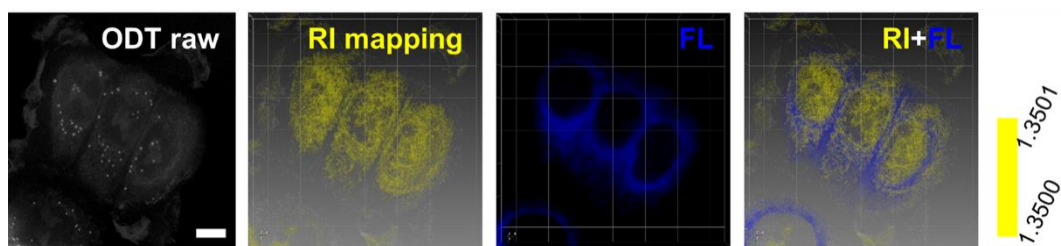


**Fig S3. Confirmation of ER region using ER tracker imaging combined with RI mapping**

Representative ODT raw and RI mapping image of MCF7 cells stained by the ER-Tracker™ Blue-White DPX is shown. The RI mapping of ER with high refractive index was carried out with reference to the region presented by the ER-Tracker. Scale bar, 10 $\mu$ m.

## 국문요약

나노입자는 물리화학적 특성을 인위적으로 조절할 수 있기 때문에 효과적인 약물 전달체로서 약물전달시스템에서 부각되고 있다. 나노입자의 물리화학적 특성 중에서 표면전하는 효율적인 세포전달을 위해 고려해야 할 중요한 요소 중 하나이다. 특히, 세포독성이 적고 효율적인 세포내 전달을 위해서 양성과 음성의 표면전하 중 어떤 전하가 적합한지 충분한 고찰이 필요하다. 최근에는 다양한 나노입자가 자가포식을 유도한다는 것이 알려져 있다. 하지만 이러한 자가포식 유도과 나노입자의 물리화학적 특성이 서로 정량적으로 어떻게 관련되어 있는지에 대해서는 아직 불분명하다. 본 연구는 이러한 정량적 관계를 단일 나노입자와 소기관 수준에서 밝혀내기 위해서, 표면전하가 서로 다르고 RITC염료를 포함하는 실리카 기반 형광자성 나노입자(Si-FMNPs)를 이용하여 세포내 유입량, 세포내 시공간적 분포, 및 세포 소기관, 특히 autophagosome과의 상호작용을 조사하였다. 초고해상도 공초점 레이저 스캐닝 현미경(CLSM)을 사용하여 시간에 따라 3차원 세포이미지를 정량적으로 분석한 결과, 양의 표면전하를 가지는 Si-FMNPs가 세포내 흡수 효율이 음의 표면전하를 가지는 Si-FMNPs보다 크다는 것과, 나노입자의 전하에 따라 자가포식과 분해과정에 대한 동역학적 특성이 크게 다르다는 것을 밝혀냈다. 또한, 양의 표면전하를 가지는 Si-FMNPs의 세포독성이 현저하게 낮은 것도 확인되었다. 한편, 형광이미징 분석을 보완할 목적으로 3차원 무표지 광회절 토모그래피 기법(ODT)을 사용하여 실시간으로 살아있는 세포의 각 소기관 별 굴절률(RI) 값을 소기관 수준에서 평가하였다. 흥미롭게도, 나노입자 처리 후 핵소체와 핵주변의 ER에서 굴절률이 크게 높아진다는 것을 확인하였다. 이러한 결

과는 나노입자가 오토파지와 상호작용 하면서 핵주변 ER에 축적되는 것과, 스트레스에 의한 핵소체의 물리적 변화에 의해 발생한 것으로 추측된다. 이러한 기법은 앞으로 형광 없이 굴절률이 높은 나노입자나 엑소좀을 세포에 처리해 세포내로 흡수되어 분해되는 전 과정을 분석하는데 응용될 수 있다. 고해상도 형광 및 무표지 이미징을 통합하여 나노입자의 세포내 시공간분석을 정량분석한 본 연구는 앞으로 효과적이고 안전한 나노전달체를 개발하는데 크게 기여할 것으로 기대한다.

**핵심단어 : 실리카 기반 나노입자, 표면전하, 흡수 및 자가 소화 작용의 동역학적 성질, 광회절 토모그래피, 굴절률**